NANOMATERIALS

10.1126/sciadv.1500661

Fingertip skin–inspired microstructured ferroelectric skins discriminate static/dynamic pressure and temperature stimuli

Jonghwa Park,[1]* Marie Kim,[2]* Youngoh Lee,[1] Heon Sang Lee,[2†] Hyunhyub Ko[1†]

In human fingertips, the fingerprint patterns and interlocked epidermal-dermal microridges play a critical role in amplifying and transferring tactile signals to various mechanoreceptors, enabling spatiotemporal perception of various static and dynamic tactile signals. Inspired by the structure and functions of the human fingertip, we fabricated fingerprint-like patterns and interlocked microstructures in ferroelectric films, which can enhance the piezoelectric, pyroelectric, and piezoresistive sensing of static and dynamic mechanothermal signals. Our flexible and microstructured ferroelectric skins can detect and discriminate between multiple spatiotemporal tactile stimuli including static and dynamic pressure, vibration, and temperature with high sensitivities. As proof-of-concept demonstration, the sensors have been used for the simultaneous monitoring of pulse pressure and temperature of artery vessels, precise detection of acoustic sounds, and discrimination of various surface textures. Our microstructured ferroelectric skins may find applications in robotic skins, wearable sensors, and medical diagnostic devices.

INTRODUCTION

Many research groups have recently demonstrated flexible electronic skins (e-skins) with high tactile sensitivities that are capable of mimicking the tactile sensing capabilities of the human skin (*1*–*14*). In particular, flexible and multifunctional e-skins can find applications in humanoid robotics (*15*), skin prosthetics (*16*), and wearable health monitoring devices (*17*). One critical requirement to using the e-skins for human skin–like tactile sensor applications is the ability to simultaneously perceive and differentiate between multiple spatiotemporal tactile stimuli such as static and dynamic pressure, temperature, and vibration. E-skins with these capabilities may enable, for example, humanoid robots that can precisely grasp and manipulate objects, discern surface texture and hardness, and feel the warmth of living objects. Although there have been several reports on the development of multifunctional e-skins that can detect and differentiate between mechanical and thermal stimuli (*1*, *5*, *14*, *18*, *19*), these approaches typically require the integration of multiple sensors on heterogeneous substrates. In addition, sophisticated layouts of interconnected lines such as open mesh and serpentine layouts are needed to minimize mechanical strain effects. Recently, e-skins that can simultaneously detect pressure and thermal variations were demonstrated in a single device fabricated using ferroelectric or graphene materials (*20*–*22*). However, only the perception of static pressure was demonstrated in these reports. In addition to the perception of static tactile stimuli, the spatiotemporal detection of dynamic tactile stimuli is critical in the recognition of slip between the skin and objects, enabling the perception of shape, hardness, and roughness (*23*). E-skins that can simultaneously detect thermal and mechanical (static and dynamic) stimuli with high sensitivities are yet to be developed.

Human skin is a complex sensory system that contains unique epidermal and dermal microstructures and sensory receptors (Fig. 1A) (*24*, *25*). Fingerprint patterns enable the perception of fine surface texture by amplifying the vibrotactile signals when the finger is scanned over a surface (*26*–*28*). The interlocked microstructures between the epidermal and dermal layers are known to amplify and efficiently transfer the tactile stimuli to cutaneous mechanoreceptors (*29*, *30*). Human skin can also detect and discriminate between static and dynamic mechanical stimuli. Within human skin, while the slowly adapting receptors (for example, Merkel and Ruffini corpuscles) respond to sustained touch and pressure on the skin, fast-adapting receptors (for example, Meissner and Pacinian corpuscles) respond to dynamic touch and vibration stimuli (*25*). In addition, human skin is known to have both piezoelectric and pyroelectric properties originating from the presence of polar keratin, elastin, and collagen fibers with unique orientations (*30*–*33*), which enable human skin to precisely perceive and differentiate mechanical and thermal stimuli. All of these microstructures and receptors enable human skin to simultaneously perceive and differentiate between multiple spatiotemporal tactile stimuli. However, such abilities for multifunctional tactile perceptions have not been demonstrated in artificial e-skins. Inspired by the epidermal-dermal interlocked microstructures in human skin, we have previously reported piezoresistive sensors with interlocked microdome arrays, which can detect various static mechanical stimuli including normal, shear, stretching, and bending forces (*34*, *35*). However, these previous sensors are based on the piezoresistive mode of operations and therefore can only detect static and low-frequency stimuli. The other sensing capabilities of human skin including texture perception by fingerprint patterns, high-frequency vibration detection by Pacinian corpuscles, and piezoelectricity and pyroelectricity of skin are also required for the detection and discrimination of various static and dynamic stimuli, temperature, and surface textures.

Here, mimicking diverse structures and functions of the sophisticated sensory system in human fingertips, we introduce human skin–inspired multimodal e-skins based on flexible and microstructured ferroelectric films (Fig. 1B), which enhance the detection and discrimination of multiple spatiotemporal tactile stimuli such as static and dynamic pressure, temperature, and vibration. The piezoelectric and

[1]School of Energy and Chemical Engineering, Ulsan National Institute of Science and Technology, Ulsan Metropolitan City 689-798, Republic of Korea. [2]Department of Chemical Engineering, Dong-A University, Busan 604-714, Republic of Korea.
*These authors contributed equally to this work.
†Corresponding author. E-mail: hyunhko@unist.ac.kr (H.K.); heonlee@dau.ac.kr (H.S.L.)

pyroelectric properties of human skin that detect dynamic touch and temperature are realized in the e-skins by using piezoelectric and pyroelectric responses of ferroelectric polymer composites composed of poly(vinylidene fluoride) (PVDF) and reduced graphene oxide (rGO). The intrinsic inability of the ferroelectric e-skins to detect sustained static pressures is overcome by using the piezoresistive change in contact resistance between the interlocked microdome arrays in the rGO/PVDF composites (*34*, *35*). In addition, to mimic the epidermal and dermal microstructures observed in human finger skin, fingerprint patterns and interlocked microstructures are used in the e-skins to amplify tactile signals by static and dynamic pressure, temperature, and vibration. We also show that the e-skin can simultaneously detect pressure and temperature variations and separately resolve these stimuli via different signal generation modes such as sustained pressure (piezoresistive), tiny and temporal pressure (piezoelectric), and temperature (pyroelectric). As proof of concept, we demonstrate that our e-skin can perceive artery pulse pressure as well as skin temperature simultaneously, besides perceiving high-frequency dynamic sound waves and various surface textures with different topological patterns, roughness, and hardness. All of these functions are highly desirable in robotics and wearable health care monitoring devices.

RESULTS

Ferroelectric rGO/PVDF composite films for temperature mapping

We fabricated flexible ferroelectric films by introducing graphene oxide (GO) sheets in the PVDF matrix and, subsequently, rod casting at a low temperature (50°C for 12 hours). At this low crystallization temperature, both PVDF/GO mixtures and pure PVDF crystallize into polar phases (β-phase). The formation of polar phases in PVDF was confirmed by x-ray diffraction (XRD) and Fourier transform infrared (FTIR) spectroscopy analyses (Section 1 in the Supplementary Materials and figs. S1 to S3). Next, to increase the conductivity of the composite films for use as piezoresistive sensors, we further reduced the GO in the composite films by annealing at 160°C for 3 hours, during which the brownish transparent film turned black (fig. S1A). Even after annealing, the polar crystal structure of PVDF is still maintained in the composite films (fig. S1A), which is not the case for pure ferroelectric PVDF made via solution casting at low temperature (fig. S1A) or made using a conventional electric poling process (*36*). This may be ascribed to the steric effect of the existence of GO sheets adjacent to crystalline PVDF and to the interaction between PVDF molecules and GO surface atoms. The solution rod casting method used in this study for fabricating ferroelectric PVDF/rGO composite films is scalable. Flexible and large-area composite films (20×15 cm^2) are easily obtained (inset in Fig. 2A). A cross-sectional scanning electron microscopy (SEM) image of the rGO/PVDF composite film with an rGO concentration of 1 weight percent (wt %) indicates that the rGO sheets are uniformly dispersed and stacked within the PVDF matrix (Fig. 2A). An increase in the rGO content in the composite further increases the tendency to form stacked rGO structures (fig. S4A).

The current-voltage (*I*-*V*) curves of the ferroelectric composite film (1 wt % rGO) as a function of temperature show that the current increases with an increase in temperature from 0° to 100°C (Fig. 2B). When the relative resistance ($\Delta R/R_0$) is plotted as a function of temperature for all the PVDF/rGO composites with various rGO contents, the resistance decreases with an increase in the temperature (Fig. 2C). This negative temperature coefficient (NTC) of resistance is not common for conductive composites, because most of them show a positive temperature coefficient behavior, owing to thermal swelling of the polymer

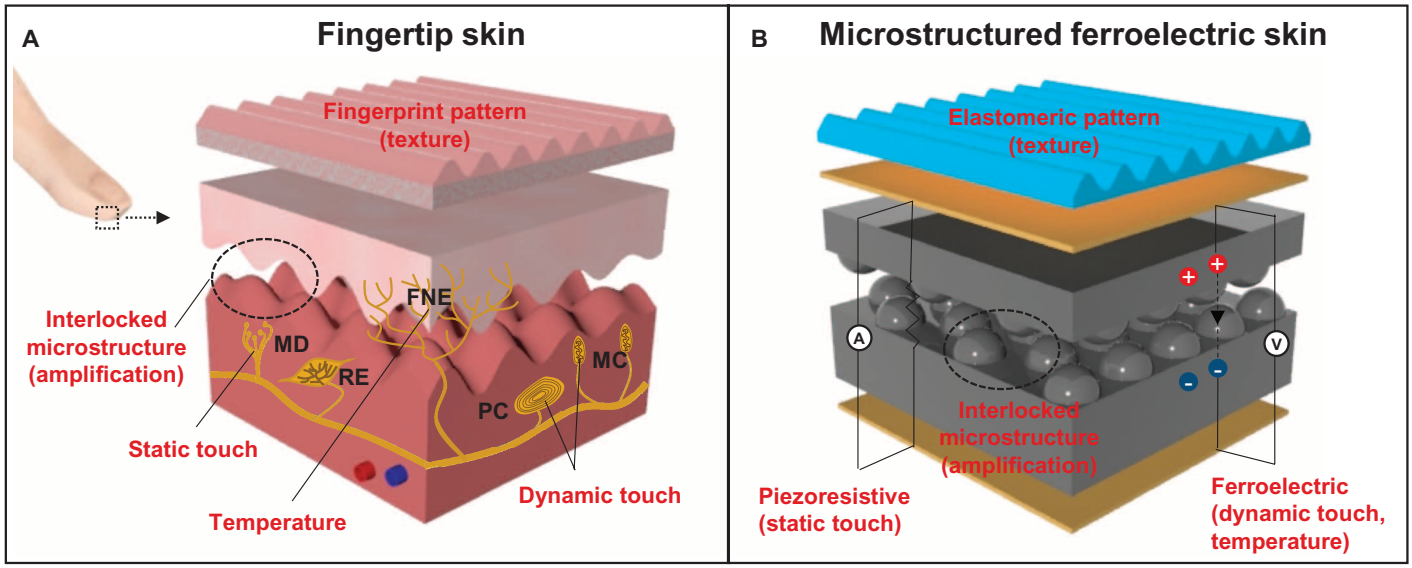

Fig. 1. Human skin–inspired multifunctional e-skin. (**A**) Structural and functional characteristics of human fingertips. Fingertip skin consists of slow-adapting mechanoreceptors [Merkel (MD) and Ruffini corpuscles (RE)] for static touch, fast-adapting mechanoreceptors [Meissner (MC) and Pacinian corpuscles (PC)] for dynamic touch, free nerve endings (FNE) for temperature, fingerprint patterns for texture, and epidermal/dermal interlocked microstructures for tactile signal amplification. (**B**) Flexible and multimodal ferroelectric e-skin. The functionalities of human skin are mimicked by elastomeric patterns (texture) and piezoresistive (static pressure), ferroelectric (dynamic pressure and temperature), and interlocked microdome arrays (tactile signal amplification).

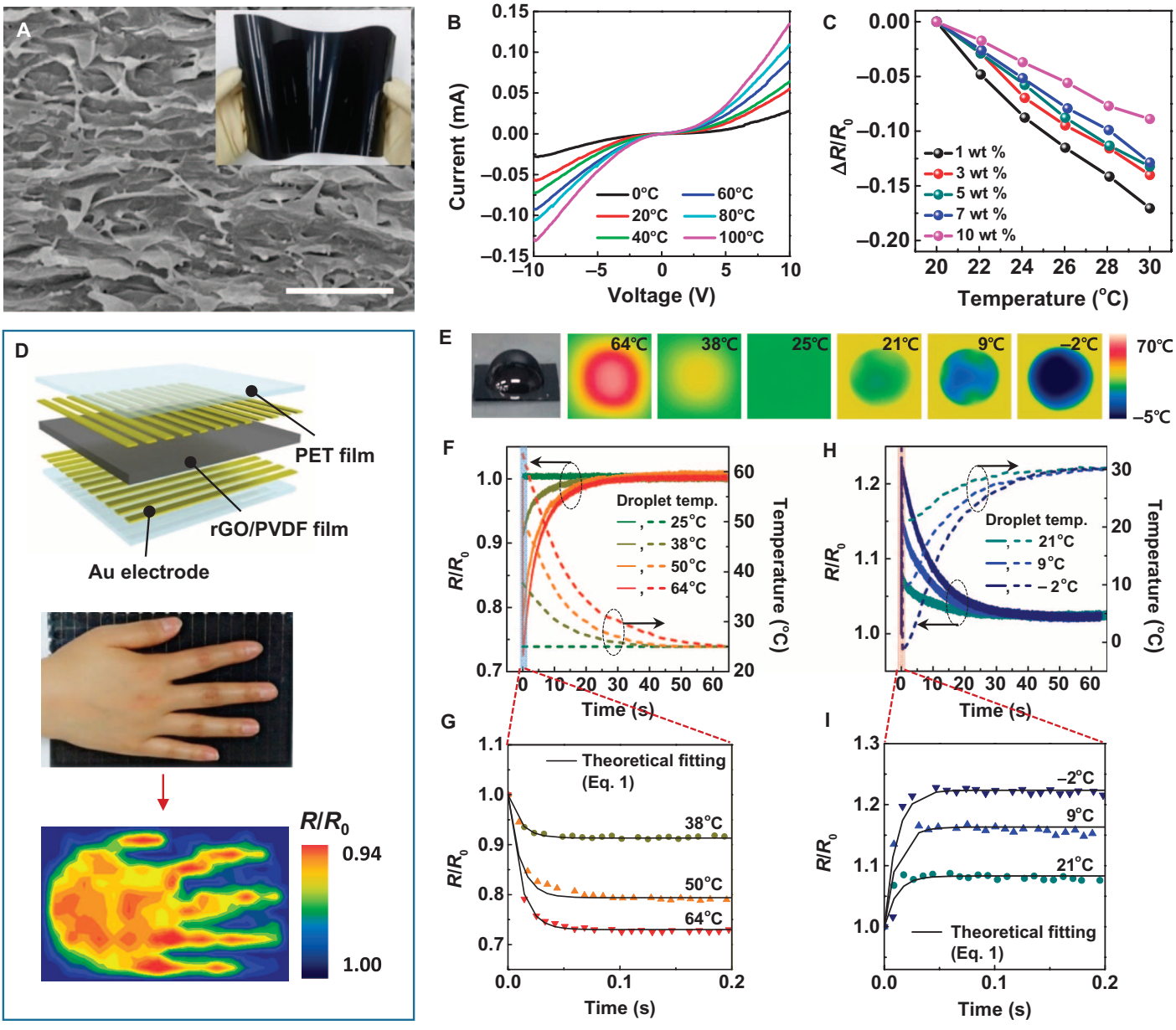

Fig. 2. Temperature-sensing properties of the flexible rGO/PVDF nanocomposite film. (**A**) Cross-sectional SEM image of the rGO/PVDF composite film with stacked GO sheets. Scale bar, 1 μm. The inset shows a photograph of a flexible and large-scale (20 × 15 cm^2) rGO/PVDF composite film. (**B**) Current-voltage curves of 1 wt % rGO/PVDF composite films at various temperatures. (**C**) Relative resistance change of rGO/PVDF composite film as a function of temperature for various concentrations of rGO. (**D**) Detection of temperature distribution on the human palm. (Top) Schematic diagram of a sensor array, where the rGO/PVDF composite film is sandwiched between gold electrode arrays (18 × 12 pixels). (Middle) Photograph of a human hand on top of the sensor array. (Bottom) Contour mapping of electrical resistance variations for the local temperature distribution on the human palm. (**E**) A representative photograph and infrared (IR) camera images of water droplets with different droplet temperatures (64° to −2°C) on the e-skins. (**F** and **H**) Relative resistance (R/R_0) and temperature (T) variations of the e-skins after contact with water droplets (F) above room temperature (25° to 64°C) and (H) below room temperature (−2° to 21°C). Temperature (T) change is measured by an IR camera. (**G** and **I**) Initial stages of time-domain signals in (F) and (H) showing the variation of relative resistance immediately after contact between e-skins and water droplets. The solid lines represent a fit derived from Eq. 1.

matrix (*37*–*39*). The NTC behavior observed in our composite film can be attributed to the change in the contact resistance between the rGO sheets (*40*) by thermomechanical variation as well as the intrinsic NTC behavior of rGO (*41*). Temperature-dependent resistance change can be quantified by means of the temperature coefficient of resistance (TCR) parameter, which is defined as TCR = $(\Delta R/R)/\Delta T$, where R is the resistance of the film and T is the temperature. TCR is reduced with an increase in the rGO content (Fig. 2C). This is attributed to the decrease in the crystallinity of PVDF with an increase in the rGO content in the composites (fig. S4, B and C). For demonstration, we fabricated

flexible temperature-sensitive e-skins by placing gold electrode arrays on the top and bottom of the film (18 × 12 pixels). When a human hand is placed on top of the e-skins, the temperature variation over the entire contact area can be mapped by the temperature sensor (Fig. 2D). This temperature mapping capability of cost-effective flexible films is beneficial for the continuous monitoring of the temperature variation of human skin, which can provide clinical information for medical diagnosis (*11*).

To further investigate the temporal response of e-skins to continuous temperature variations, we analyzed the dynamic changes in e-skin resistance immediately after contact with a water droplet at various temperatures. Figure 2E shows a representative optical image and infrared camera images of water droplets on e-skins with different droplet temperatures. The solid lines in Fig. 2 (F and H) show the time-dependent resistance change of the e-skins, whereas the dashed lines show the droplet temperatures, as monitored by an IR camera. When a water droplet at room temperature (25°C) falls on the e-skin at 25°C, the electrical resistance of the e-skin does not change (Fig. 2F). On the other hand, the falling of warm water droplets (38°, 50°, and 64°C) induces an instantaneous decrease in the relative resistance to 0.74 to 0.92 (Fig. 2G). Although the resistance rapidly decreases immediately after contact with the warm water droplets, it then gradually increases because of the cooling of the warm water droplet over time and finally reaches the original value of 1 at thermal equilibrium. On the other hand, the falling of cold water droplets (−2°, 9°, and 21°C) on the e-skins at 36°C shows the opposite behavior (Fig. 2H). In this case, the relative resistance instantaneously increases immediately after contact with the cold water droplets and then gradually decreases because of the warming up of the droplet to a local steady-state temperature. Here, the relative resistance at a local steady state (R/R_0 = 1.02) is slightly higher than the original value (R/R_0 = 1.00), which can be attributed to the temperature difference between the water droplet at local steady state (30°C) and the original e-skin temperature (36°C). The local steady-state temperature (30°C) of a water droplet can be reached owing to the temperature difference between the e-skin (36°C) and the atmosphere (25°C). When the water droplet is removed from the e-skin surface, the relative resistance recovers to the original value (fig. S5). This result verifies that the e-skin can also detect a wetting state by cold water. For both the warm and cold water droplet measurements, the instantaneous and subsequent gradual variations in the relative resistances (solid lines) agree with the temperature variation behavior of the water droplets. The instantaneous variation in the resistance leads to local equilibria in the initial time domain (<0.2 s) after water contact (Fig. 2, G and I). This behavior can be modeled as follows (Eq. 1)

$$\frac{R}{R_0}(t) = \left(\frac{R}{R_0}\right)_{\text{L.E.}} + \left[1 - \left(\frac{R}{R_0}\right)_{\text{L.E.}}\right]\exp\left(-\frac{t}{\tau_T}\right) \quad (1)$$

where R is the resistance of the e-skin, t is the time, and τ_T is the characteristic time (Section 2 in the Supplementary Materials). The experimental data fit well to Eq. 1 with τ_T = 11 ms for both the warm and cold water droplets (Fig. 2, G and I). The τ_T value of 11 ms corresponds to the time scale required for the overall system composed of the e-skin and water droplet to reach local thermal equilibrium (Section 3 in the Supplementary Materials). The above results demonstrate that our e-skins enable fast and precise monitoring of temporal and spatial changes in temperature.

Simultaneous detection of static pressure and temperature

The planar composite film is not sensitive to the minute pressure variations induced by the water droplet on the e-skin. The pressure sensitivity can be significantly enhanced by using an interlocked geometry of microdome arrays in the laminated composite films (Fig. 3A). In this case, an external stress can induce deformation, which, in turn, can induce variation in the contact area between the interlocked microdomes, resulting in pressure-dependent variation of contact resistance. Figure 3B confirms that the pressure sensitivity of the interlocked microdome arrays is significantly higher than that of a planar film mainly because of the large change in contact area between neighboring microdome arrays under external stress (*34*, *35*). The contact resistance of interlocked microdome arrays continuously decreases with the increase of pressure up to 49.5 kPa, which indicates the wide dynamic range of pressure detection (fig. S6). We also note that a decrease in the loading of rGO in the film improves sensitivity, which can be attributed to the increased softness (fig. S4D) and piezoelectric effects associated with the decrease in the rGO content. The e-skins can detect the tiny static pressure (~0.6 Pa) of a human hair pushing or dynamic movements of hair drawing on the e-skin (fig. S7A). Furthermore, e-skins enabled the sensitive monitoring of air flow pressure variations ranging from 0.6 to 2.2 Pa (fig. S7B). For repetitive cycles (5000 times at 0.3 Hz) of normal force (20 kPa), the e-skin shows no noticeable degradation (fig. S8).

The geometry of the interlocked microdome array also results in a higher TCR value (2.93%/°C) compared to the planar film (1.58%/°C) (Fig. 3C). For interlocked microdome structures, in addition to the intrinsic NTC behavior of the composite films, thermal expansion and softening of the PVDF matrix lead to increased contact area and, thus, decreased contact resistance, resulting in enhanced NTC behavior. The TCR value decreases with an increase in the normal pressure on the interlocked microdome arrays (fig. S9), indicating the critical role of the initial contact area in modulating the TCR values. Without normal pressure, the initial contact area is very small. However, the contact area can be significantly increased by the thermal expansion of PVDF, resulting in a decrease in resistance. This effect decreases with an increase in the initial contact area with the application of normal pressure. Therefore, the TCR value of 3.15%/°C under zero pressure significantly decreases to 1.2%/°C at a normal pressure of 1.2 kPa (fig. S9). The TCR values of interlocked microdome arrays are higher than those of film-type thermal sensors, such as carbon nanotube films (1 to 2.5%/°C at −173° to 57°C) (*42*), multiwalled carbon nanotubes/graphene flakes (0.08%/°C at 0° to 30°C) (*43*), and graphene nanoplatelets (0.0371°C at 10° to 60°C) (*44*).

To evaluate the temporal response of interlocked e-skins to continuous temperature and pressure variations at the same time, we analyzed the time-dependent variation of e-skin resistance and water temperature immediately after the falling of a water droplet (2 Pa) at various temperatures (Fig. 3D). The falling of a room-temperature water droplet on the e-skin results in a decrease in the relative resistance to 0.92, owing to the pressure applied by the water droplet (Fig. 3E). When warm water droplets at 40° and 60°C fall on the e-skin, the resistance instantaneously decreases to 0.38 and 0.25, respectively, owing to both pyroelectric and piezoresistive effects, then gradually increases because of the cooling of the warm water droplet over time, and finally reaches the resistance value of 0.92 at thermal equilibrium, which corresponds to the static pressure applied by the water droplet. When the water droplet pressure is changed (Fig. 3F), the equilibrium value of relative

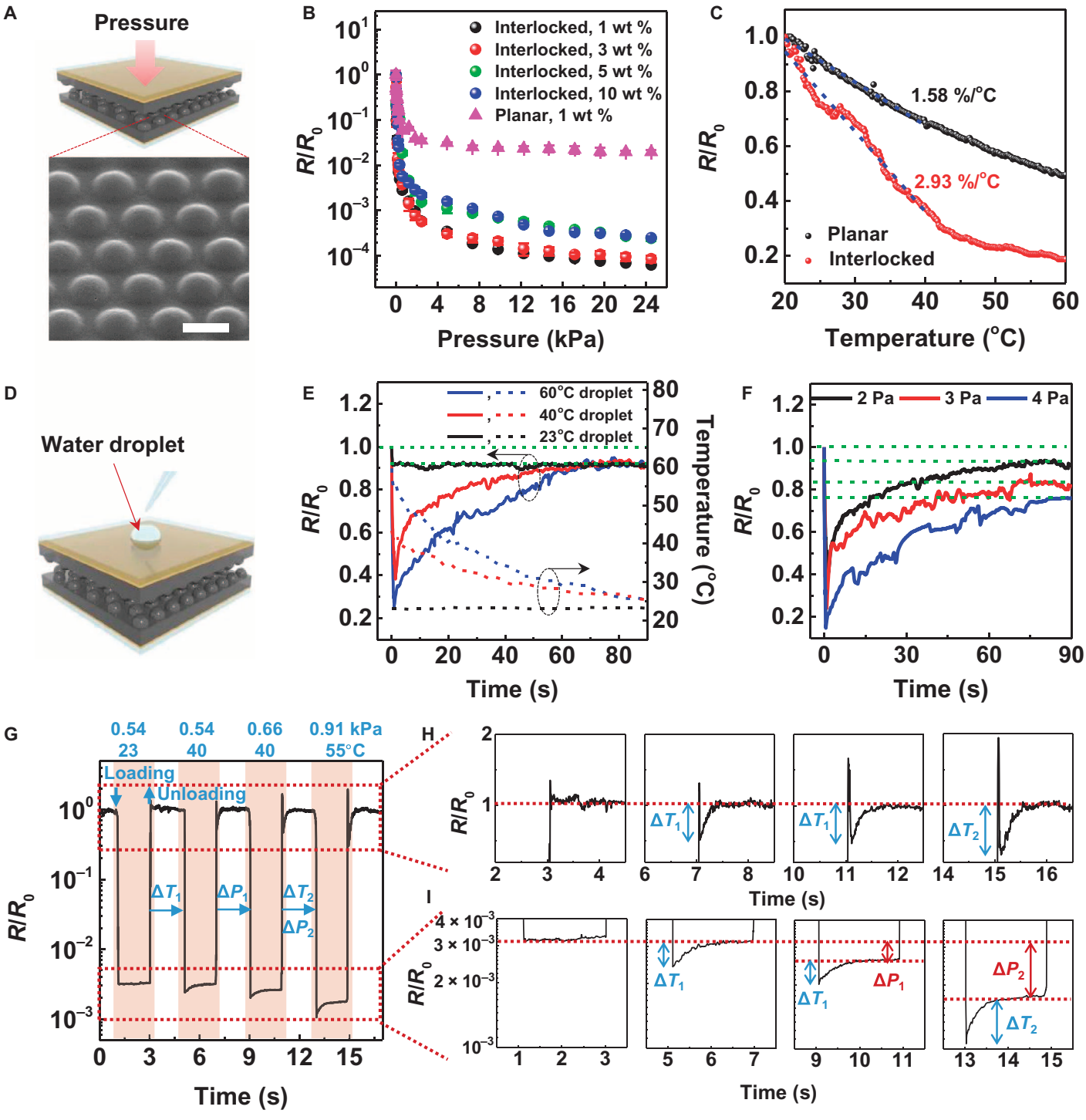

Fig. 3. Piezoresistive e-skin with interlocked microdome arrays for simultaneous detection of static pressure and temperature. (**A**) Schematic illustration of the e-skin with interlocked microdome array. A tilted SEM image shows the microdome arrays that are 10 μm in diameter, 4 μm in height, and 12 μm in pitch size. Scale bar, 10 μm. (**B**) Relative resistances of e-skins with interlocked microdome (circle) and single planar (triangle) geometries as a function of applied pressure for different rGO loading concentrations. (**C**) Relative resistances of e-skins with interlocked microdome (red) and single planar (black) geometries as a function of temperature for 1 wt % rGO. (**D**) Schematic illustration of the loading of a water droplet onto the e-skin. (**E** and **F**) Time-dependent variation of relative resistances and temperature immediately after the loading of water droplets on e-skins at (E) different temperatures (droplet pressure, 2 Pa) and (F) different pressures (droplet temperature, 40°C). (**G**) Time-dependent variation of relative resistances after the loading/unloading cycles of objects with various pressure and temperature values on top of an interlocked e-skin. (**H** and **I**) Magnified variation of relative resistances at the moment of loading/unloading cycles in (G) showing the detection and discrimination of simultaneous temperature and pressure variations.

resistance is different for different pressure values. To further demonstrate the discrimination of temperature and pressure variations of different types of objects, we performed loading/unloading cycles of water-filled glass vials with various pressure and temperature values on top of an interlocked e-skin (Fig. 3G). While the first loading/unloading signals in response to 0.54 kPa pressure at 23°C exhibit only equilibrium values of relative resistance due to the absence of thermal gradient with the e-skin, the gradual resistance change is additionally observed on top of equilibrium values at the moments of loading (Fig. 3I) and unloading (Fig. 3H) cycles due to the thermal gradient and the subsequent equilibrium processes. Here, the differences between instantaneous and equilibrated resistance values increase with the increase of temperature, demonstrating the detection of temperature variations. When the pressure is simultaneously varied in addition to temperature variation, the pressure variation can be monitored by the difference between equilibrated resistance values (Fig. 3I), which can be distinguished from instantaneous resistance variation due to temperature change. These results demonstrate that the interlocked ferroelectric e-skins can simultaneously detect and discern temperature and pressure variations as a result of their piezoresistive and pyroelectric properties.

Simultaneous monitoring of artery pulse pressure and temperature

The pulse waveform of the radial artery can be used for real-time and noninvasive diagnosis of cardiovascular problems associated with arteriosclerosis, hypertension, and diabetes (*45*). In particular, because blood pressure is easily influenced by environmental changes, wearable blood pressure monitoring devices are required for the measurement of average daily blood pressure to accurately analyze cardiovascular problems (*46*). Although capacitive (*47*, *48*), triboelectric (*49*), piezoresistive (*12*, *50*), and piezoelectric (*51*) pressure sensors have been introduced as wearable devices for the detection of artery pulse pressure, there have been no reports on the simultaneous detection of artery temperature and pressure. Information on the wrist skin temperature during the measurement of artery pulse pressure is critical in the accurate analysis of pulse waveforms because heat and cold stresses affect the vasoconstriction and vasodilation of blood vessels, which results in variation in arterial stiffness and radial pressure (*52*). Our interlocked e-skin enables the simultaneous monitoring of temperature and artery pulse pressure when attached onto the wrist skin (Fig. 4A). Depending on the skin temperature, the blood vessel undergoes vasodilation or vasoconstriction, which results in a decrease or increase in the pulse pressure, respectively (inset in Fig. 4A). Figure 4B shows the typical piezoresistive readout of wrist pulse pressure. Three distinguishable peaks (P_1, P_2, and P_3) are observed (*53*). Here, P_1 (pulse pressure) is due to the blood flow ejected by heart contraction and is the difference between the systolic (P_{Sys}) and diastolic (P_{Dia}) pressures. On the other hand, P_2 and P_3 (reflected wave pressures) are generated by reflected waves from the peripheral sites (hand for P_2 and lower body for P_3).

The shape of the artery pulse wave is variable depending on the arterial stiffness, pulse wave velocity (PWV), and reflected waves. For individuals with hypertension and for aged persons, the systolic and pulse pressures are augmented, owing to increased arterial stiffness, which causes increased PWV and early return of reflected waves (*53*). For the quantitative evaluation of arterial stiffness, the radial artery augmentation index ($AI_r = P_2/P_1$), radial diastolic augmentation ($DAI = P_3/P_1$), and round-trip time of a reflected wave from the hand periphery (T_R) are commonly used (*53*, *54*). In Fig. 4C, before physical exercise, the average values (from five pulse waves) of AI_r and DAI under normal conditions are observed to be 0.45 and 0.31, respectively, which are consistent with the data provided in the literature on healthy 29-year-old males (*53*). After physical exercise, the pulse rate increases to 84 beats/min from 72 beats/min under normal conditions and the pulse intensity increases as a result of increased cardiac output to rapidly provide blood to the activated muscles. In addition, owing to vasodilation of the muscular arteries after exercise, P_2 is reduced, resulting in a decrease in the augmentation index ($AI_r = 0.36$, $DAI = 0.21$), indicating decreased arterial stiffness. We also observe that the relative resistance decreases to 0.94, owing to the increase in skin temperature after exercise.

To investigate the skin temperature–dependent variation of pulse pressure of the radial artery, we used the interlocked e-skin to acquire the arterial pulse pressure immediately after immersion of the hand into a water bath at various temperatures (20° to 42°C) for 2 min. With the increase in skin temperature from 20° to 42°C, the relative resistance of diastolic pressure (P_{Dia}) decreases from 1.40 to 0.65 (Fig. 4D). In addition, the arterial pulse pressure shows different waveforms depending on the temperature (Fig. 4E). Here, all the pulse and reflected wave pressures (P_1, P_2, and P_3) decrease with an increase in the temperature. Detailed analyses of the variations in the pulse waveforms are shown in Fig. 4F. The relative resistance linearly decreases with an increase in skin temperature, which results in a slope of 3.3%/°C, which is close to the TCR value (2.93%/°C) of the interlocked e-skin (Fig. 3C). This linear relationship between resistance and temperature can be used to directly monitor the skin temperature during the measurement of arterial pulse pressure. With an increase in skin temperature from 20° to 42°C, the values of AI_r and DAI decrease from 0.54 and 0.31 to 0.27 and 0.09, respectively. This phenomenon could be attributed to the cold stress– and heat stress–induced vasoconstriction and vasodilation of blood vessels in the radial artery under normal conditions (skin temperature of 32°C), which results in an increase (or decrease in the case of heat stress) in arterial stiffness, and thus an increase in the blood pressure, reflection wave, and PWV (*55*). In addition, T_R increases from 142 to 248 ms with an increase in temperature. The increase in the delayed time of the reflective wave with the increase in temperature is attributed to reduced cardiac output and increased compliance of the blood vessel (arterial stiffness). Compared to traditional arterial tonometry with only pressure-sensing functions (*54*), the interlocked e-skin, which has both pressure- and temperature-sensing capabilities, could raise the accuracy of blood pressure monitoring by accounting for skin temperature.

Piezoelectric e-skins for detection of dynamic touch and acoustic waves

Our ferroelectric e-skins with interlocked geometry also enable piezoelectric perception of dynamic tactile stimuli. Compared to planar piezoelectric films, the interlocked e-skin with a larger contact area and stress concentration effects at the small contact spots between the microdomes can induce a larger deformation and thus a higher piezopotential, resulting in improvements in piezoelectric performance (Fig. 5A) (*56*). The addition of GO into PVDF can enhance piezoelectricity, but further reduction of GO into rGO decreases piezoelectricity (Fig. 5B). We observed that the increase of film conductivity with the increase of rGO reduction time resulted in the decrease of piezoelectric performance (fig. S10). This behavior can be attributed to the enhanced

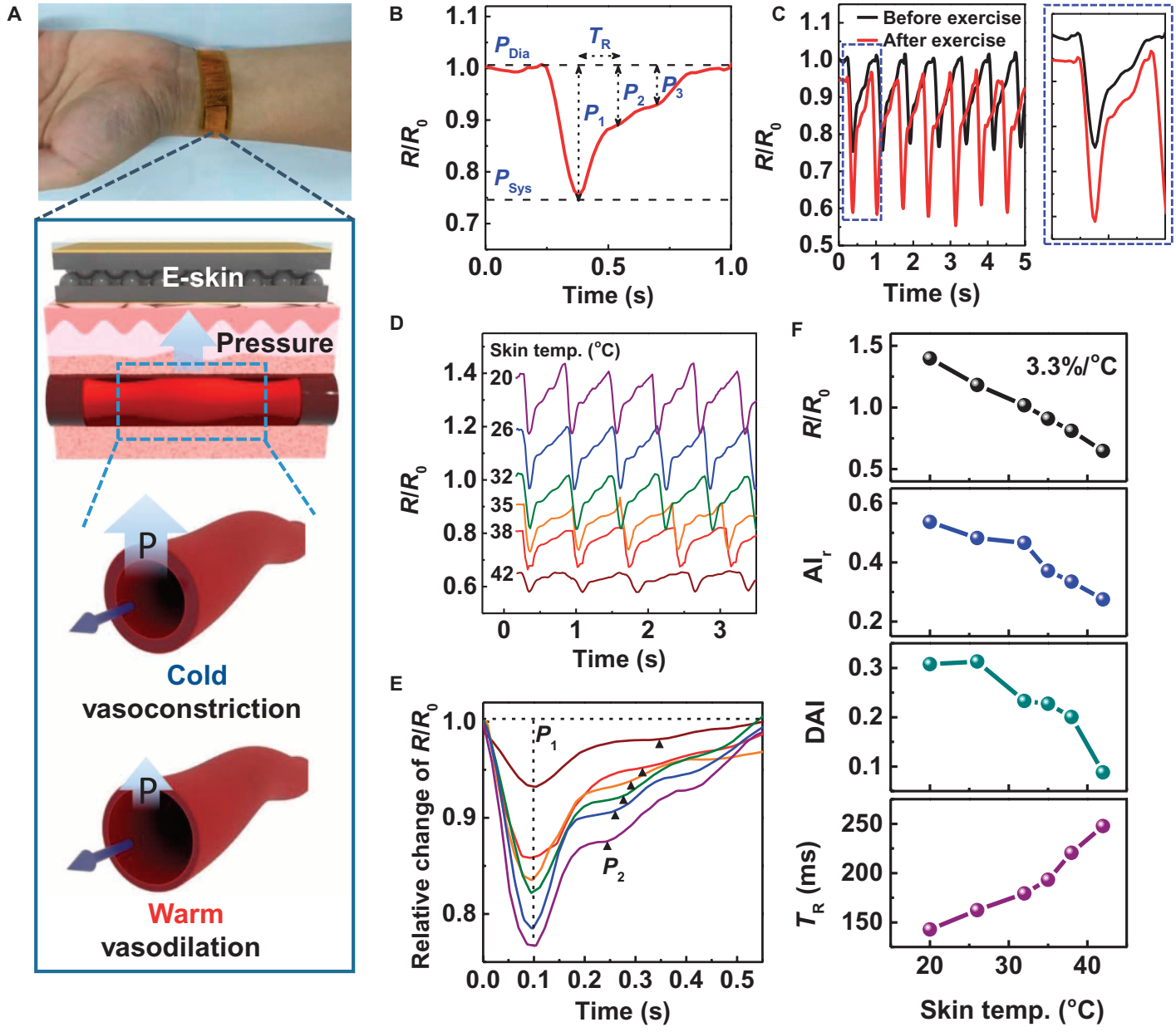

Fig. 4. Piezoresistive e-skin with interlocked microdome array for simultaneous monitoring of artery pulse pressure and temperature. (**A**) Photograph of a wearable e-skin for monitoring artery pulse pressure and temperature. The enlarged schematic illustrations indicate the effect of temperature on the constriction (cold) and dilation (warm) of arterial vessels. (**B**) Relative resistance variations in response to artery pulse pressure. The pulse pressure waveform consists of three peaks corresponding to pulse pressure (P_1) and reflected wave pressures from the hand (P_2) and lower body (P_3). P_1 is the difference between the systolic (P_{Sys}) and diastolic (P_{Dia}) pressures. (**C**) Variation of the pulse pressure waveforms before (black) and after (red) physical exercise. (**D**) Relative resistance change of the artery pulse pressure waveforms as a function of skin temperature (20° to 42°C). (**E**) Comparison of the variation of artery pulse pressure waveform at different skin temperatures. The data in (D) are used with the data-offset modification for the comparison. (**F**) The blood pressure and temperature information acquired from the measurements in (E); variations of relative resistance (R/R_0) (black), radial artery augmentation index ($AI_r = P_2/P_1$) (blue), radial diastolic augmentation index ($DAI = P_3/P_1$) (green), and round trip time for the reflected wave from the hand periphery (T_R) (purple) as a function of skin temperature.

screening of piezoelectric polarization with the increase of film conductivity (*57*, *58*). The piezoelectric current of the interlocked microdome films depends on the applied normal forces with a sensitivity of 35 μA/Pa below 2.45 kPa and 5 μA/Pa in the range of 2.45 to 17.15 kPa (Fig. 5B). The piezoelectric current and voltage gradually increase with an increase in the applied impact frequency (0.1 to 1.5 Hz) (Fig. 5C). This behavior can be attributed to the viscoelastic property of PVDF polymers, in which the dynamic modulus increases with the increase of frequency (*59*). Because the piezoelectric current and voltage are known to be proportional to the elastic modulus of piezoelectric materials (*60*),

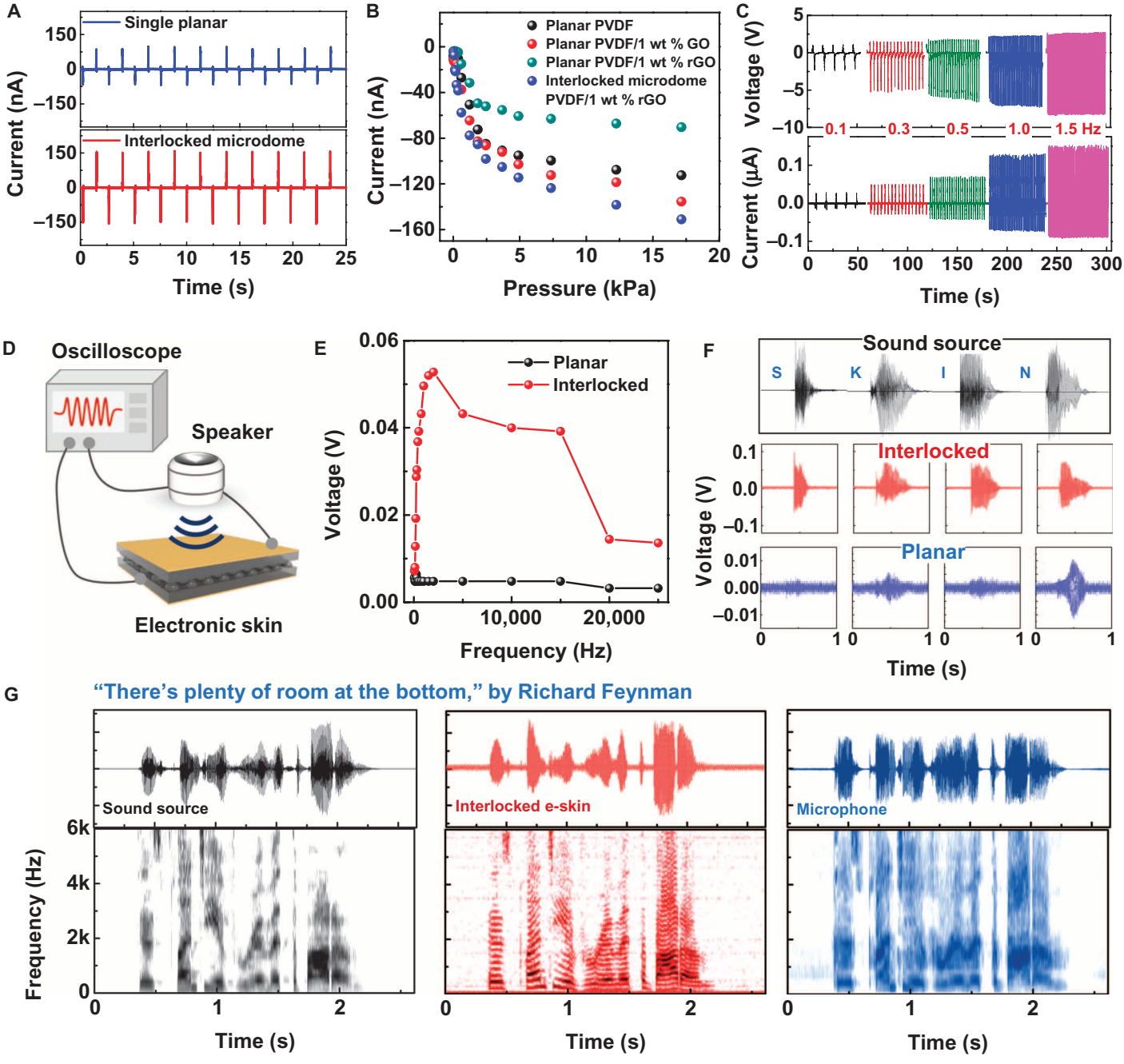

Fig. 5. Piezoelectric e-skin with interlocked microdome array for dynamic touch and acoustic sound detection. (**A**) Piezoelectric output currents of e-skins with (top) interlocked microdome array and (bottom) single planar geometries. (**B**) Pieozoelectric pressure sensitivities of the e-skins fabricated with different materials and device structures (frequency of loading pressure, 0.5 Hz). (**C**) Piezoelectric output voltage and current under repetitive impact pressure loadings at different frequencies (0.1 to 1.5 Hz) for the static normal loading force of 8.56 kPa at a fixed pushing distance of pushing tester. (**D**) Schematic illustration of the sound detection tests using the piezoelectric e-skins at the sound intensity of 96.5 dB. The sensor distance from the speaker is 2 cm. (**E**) Variation of the piezoelectric voltage in response to acoustic waves of different frequencies. (**F**) The waveforms of acoustic sound for different letters of the alphabet ("S," "K," "I," and "N") (black). The readout voltage signals from the interlocked microdome (red) and planar e-skins (blue). (**G**) The waveform and short-time Fourier transform (STFT) signals of the original sound ("There's plenty of room at the bottom," black) extracted by the sound wave analyzer, readout signals from the interlocked e-skin (red), and microphone (blue).

the increase of frequency results in the increase of piezoelectric output. The piezoelectric current is also dependent on the strain rate, which leads to the increase of piezoelectric current with the increase of frequency (*61*). In addition, the slow adjustment of the piezoelectric charges to balance the piezoelectric potential can also lead to frequency-dependent piezoelectric output (*61*, *62*). This frequency-dependent increase in the piezoelectric output could find applications in self-powered systems (*62*), accelerometers, and vibrometers (*63*). Although the piezoelectric e-skins are insensitive to sustained static pressure, the instantaneous generation of piezoelectric current enables the detection of rapid variation in dynamic forces. Figure S11 shows piezoelectric and piezoresistive signal variations of the e-skins in response to applied pressure (8.56 kPa) with different impact frequencies (0.3 to 5.0 Hz). Although both the piezoelectric and piezoresistive responses follow dynamic pressure loadings for frequencies below 3.3 Hz, for frequencies higher than 5 Hz, only the piezoelectric signals properly respond to the dynamic pressure loadings.

The instantaneous deformation and relaxation of interlocked microdome arrays and the subsequent changes in the piezoelectric currents enable the detection of sound waves consisting of high-frequency vibrations. To demonstrate the sound detection capabilities, we monitored sound waveforms from a speaker with the interlocked e-skins (Fig. 5D). The piezoelectric voltage of the interlocked e-skin increases with an increase in the sound frequency, reaches a maximum value at 2000 Hz, and then gradually decreases (Fig. 5E). On the other hand, planar e-skins do not exhibit any noticeable changes in the piezoelectric voltage. Figure 5F shows the piezoelectric voltage waveforms observed in response to the sounds of various letters of the alphabet such as "S," "K," "I," and "N" from a speaker. Although the time-dependent variation of the voltage waveforms of the interlocked e-skins precisely matches the acoustic waveforms from the speaker, the planar e-skins are unable to monitor the time-dependent variation of the acoustic waveforms. The well-known speech titled "There's plenty of room at the bottom" by R. Feynman was played to the interlocked e-skins over a commercial microphone to demonstrate the monitoring of a full sentence of acoustic waveforms (Fig. 5G). The time-dependent position and intensity of the piezoelectric voltage waveforms and the corresponding spectrograms agree with the acoustic waveforms and spectrograms of the acoustic sound of the sentence. A commercial microphone, on the other hand, cannot exactly monitor the time-dependent variation of acoustic waveforms and spectrograms of the sentence.

Piezoelectric e-skins with fingerprint-like patterns for texture perception

The rapidly adaptive piezoelectric e-skins enable the spatial and temporal encoding of tactile signals, which facilitate the perception of surface textures. For this purpose, e-skins were attached to a microstage (Fig. 6A, middle) and scanned over a surface texture (Fig. 6A, bottom) at different scanning speeds. In particular, mimicking the fingerprint patterns on human hands, we used parallel ridges (pitch, 470 μm; ridge width, 163 μm) on the surface of the e-skins (Fig. 6A, top) to amplify of texture-induced vibrations (*64*). Figure 6B displays the time-dependent variation of piezoelectric currents when the interlocked e-skin is scanned over a surface texture with parallel line patterns at different scanning speeds (0.25 to 2.5 mm/s). In addition to the oscillatory piezoelectric currents, periodic spikes (red arrows) in current are observed, owing to the regular topological features on the scanned surface (*26*). The intervals between the regular spike peaks decrease with an increase in the scanning speed. FFT spectra of these piezoelectric current signals indicate that there are fundamental frequencies (arrows) associated with each scanning speed and harmonics with decreasing amplitudes (Fig. 6C) (*65*). The fundamental frequency agrees with the spatial frequency ($f = v/\lambda$) of the line patterns (grating period of 500 μm), which is determined by the scanning speed (v) and grating period (λ) (*28*, *65*).

The STFT of the current signals further describe the time-dependent variation of the piezoelectric currents (Fig. 6D). Scanning on the regular surface patterns induces periodic line patterns with respect to time in the frequency range below 30 Hz, the number of which increases with an increase in the scanning speed in the same time domain. At frequencies higher than 100 Hz, a specific frequency is observed for the entire time domain, which can be attributed to the vibrotactile signals induced by the small features on the surface (fig. S12). The frequency position increases with an increase in the scanning speed. Both the fingerprint-like patterns and interlocked structures are critical in enhancing the perception of surface textures. The regular spike peaks in the piezoelectric currents and the corresponding periodic lines in STFT cannot be observed for the interlocked e-skins without the fingerprint-like patterns (fig. S13). Although we observe periodic current peaks for the planar e-skins with fingerprint-like patterns, the intensities of the peaks in this case are lower than those for the interlocked geometry. For planar e-skins without fingerprint-like patterns, we do not observe any unique features in the surface texture–dependent frequency variation. When the moduli of regular surface patterns are varied, our e-skins can also discriminate the variation of surface hardness/softness (fig. S14). The visibility of periodic line patterns in the STFT spectrum attenuates with the decrease of modulus. The interlocked e-skins with fingerprint-like patterns can also detect various surfaces with different roughnesses (Fig. 6E). Continuous scanning on sandpaper, paper, and glass surfaces results in different STFT features, with the rougher surface (sandpaper) exhibiting features with high amplitudes covering all frequencies below 30 Hz and the smoother surface (glass) not exhibiting any noticeable frequency features. The texture perception capability of the e-skins also enables the perception of different surfaces on our hands (fig. S15A). The e-skins can even perceive different surfaces on the hair, facial skin, and whisker regions of our head (fig. S15B).

In the tactile perception of human skin, the principal mechanoreceptor involved in the recognition of the surface texture changes depending on the element size of the texture. Slow-adapting mechanoreceptors (Merkel Disk) perceive coarse roughness with an element size of greater than 100 μm, whereas fast-adapting mechanoreceptors (Pacinian corpuscle) change under fine roughness with an element size of less than 100 μm (*66*). To investigate the perception of fine textures, we scanned e-skins (scanning speed of 2.5 mm/s) over silicon substrates with different surface patterns and sizes [line: pitch size (P) = 80 μm, width (W) = 10 μm; square: P = 80 μm, W = 20 μm; pentagon: P = 90 μm, W = 20 μm] (Fig. 6F). Scanning across silicon line patterns in the perpendicular direction (Fig. 6F, ii) induces periodic output current waves (Fig. 6F, middle) and exclusive frequency bands near 30 Hz in the STFT spectrogram (Fig. 6F, bottom), which are recognizable when compared to the smooth silicon surface (Fig. 6F, i). The 30-Hz frequency band observed at a scanning speed of 2.5 mm/s corresponds to a pitch of 83 μm, which is close to the interridge distance of 80 μm. Scanning over the silicon line pattern in the parallel direction (Fig. 6F, iii), on the other hand, does not result in a prominent frequency band near 30 Hz. The square pattern (Fig. 6F, iv) generates frequency bands near 30 Hz, which are similar to the bands observed by

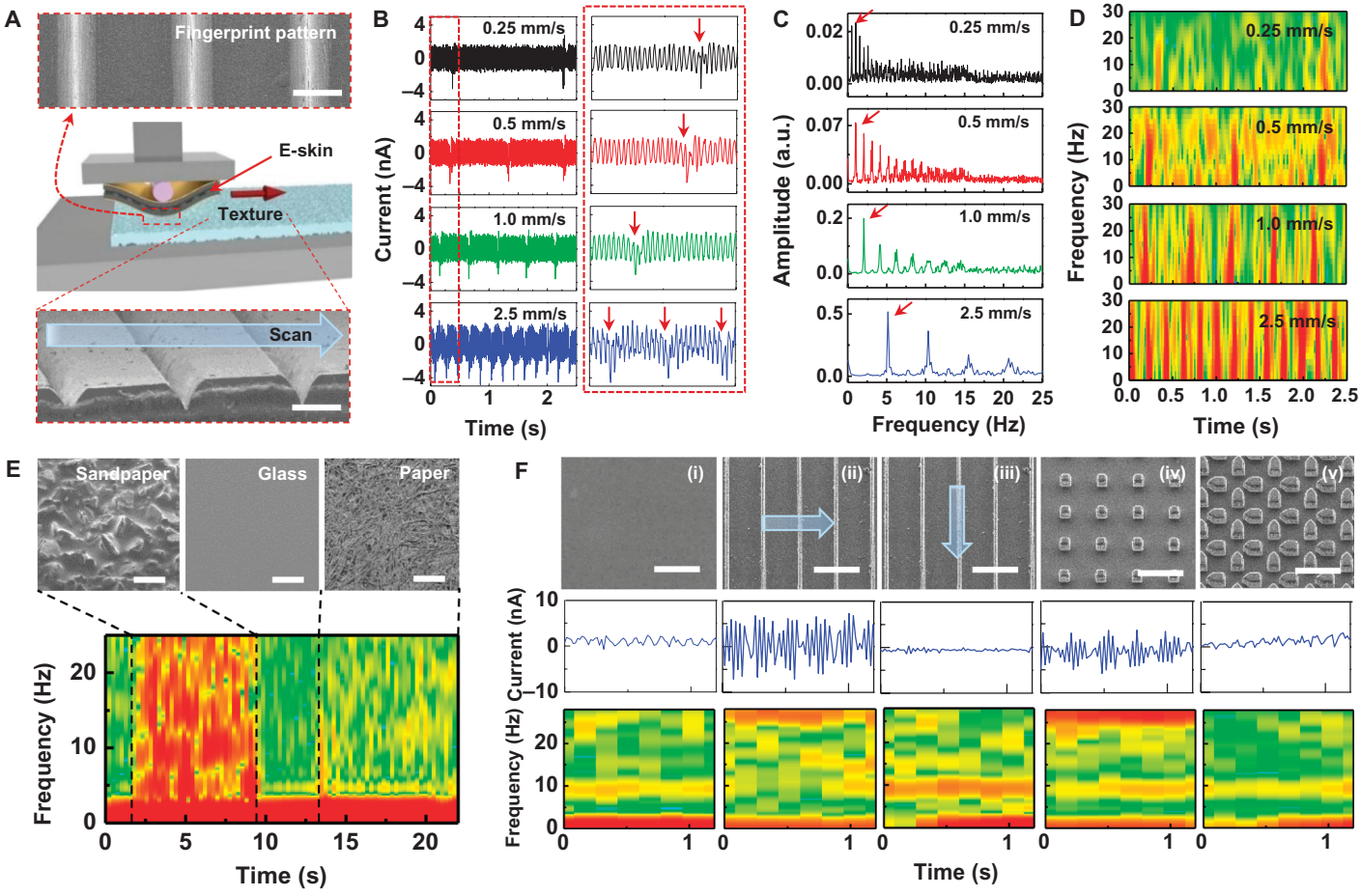

Fig. 6. Piezoelectric e-skin with fingerprint-like patterns for texture perception. (**A**) Schematic illustration of texture perception measurements, for which the e-skin is attached to a microstage and scanned over a surface. (Top) SEM image of the fingerprint-inspired PDMS pattern. (Bottom) SEM image of the PDMS substrate with periodic line patterns ($P = 470$ μm, $W = 163$ μm). Scale bar, 200 μm. (**B**) Time-dependent variation of piezoelectric currents when the e-skin is scanned over the patterned surface at different scanning speeds (0.25 to 2.5 mm/s). (**C**) Fast Fourier transform (FFT) spectra of time-dependent piezoelectric current signals in (B). (**D**) STFT spectrograms of the piezoelectric current signals in (B) for the low-frequency range (0 to 30 Hz). (**E**) Perception of texture with different roughnesses. (Top) SEM images of the sandpaper, paper, and glass surfaces. (Bottom) STFT spectra of the corresponding output currents when the e-skin is scanned at 2.5 mm/s. Scale bar, 200 μm. (**F**) Perception of fine textures (<100 μm). (Top) SEM images, (middle) output current signals, and (bottom) STFT spectra of different silicon substrates with (i) planar, (ii and iii) line pattern ($P = 80$ μm, $D = 10$ μm), (iv) square pattern ($P = 80$ μm, $D = 20$ μm), and (v) pentagon pattern ($P = 90$ μm, $D = 20$ μm). The arrow indicates the scanning direction. Scale bar, 100 μm. a.u., arbitrary units.

perpendicular scanning on the line pattern. On the other hand, scanning on the pentagon pattern (Fig. 6F, v) without any continuous interpattern gaps does not result in any noticeable frequency band near 30 Hz. We also observe a weak frequency band near 10 Hz for all the surfaces, which can be attributed to the stick-slip motions between the polydimethylsiloxane (PDMS) and silicon substrates (*67*). This stick-slip frequency near 10 Hz cannot be observed when the scanning speed is increased to 5 mm/s (fig. S16). These results indicate that the perception of fine and regular texture is only possible when continuous interpattern gaps exist in the scanning direction.

DISCUSSION

In conclusion, we have demonstrated the functionality of human skin–inspired multimodal e-skins that enable spatiotemporal recognition of static/dynamic tactile stimuli (pressure, temperature, and vibration). The design of our e-skin involves the fabrication of microstructures of ferroelectric rGO/PVDF composite films with interlocked microdome arrays and fingerprint-like microridges on the surface of the films, which enhance the piezoelectric, pyroelectric, and piezoresistive sensing capabilities of the ferroelectric composite films for static and dynamic tactile and thermal signals. Compared to planar ferroelectric films, we have shown that the geometry of the interlocked microdome arrays significantly enhances the tactile sensitivities, enabling the detection of minute variations in temperature, pressure, and acoustic vibration. Furthermore, the use of fingerprint-like microridges on top of the interlocked e-skins has been shown to significantly enhance the vibrotactile signals when the e-skins are scanned over a textured surface, enabling the perception of surface textures with various roughness and pattern shapes. For proof-of-concept demonstrations, we showed the temperature-dependent pressure monitoring of artery vessels, high-precision acoustic sound detection, and surface texture recognition of various surfaces. All of these capabilities provide a solid

platform for the application of the e-skins fabricated in this study in humanoid robotics, flexible sensors, and wearable medical diagnostic systems.

MATERIALS AND METHODS

Material synthesis

The synthesis of GO was initiated by adding graphite powder (2 g) into a solution containing H_2SO_4 (20 ml), $K_2S_2O_8$ (1 g), and P_2O_5 (1 g) at 353 K, followed by cooling the dark blue mixture to 293 K for 5 hours. Distilled water (1 liter) was added to the mixture. The mixture was then filtered and the residue on the filter was washed until the pH of the rinse water reached 7. Next, the product was dried overnight at ambient temperature in air. After preoxidation, the oxidized graphite powder (2 g) was added to H_2SO_4 (75 ml) at 273 K in an ice bath. $KMnO_4$ (10 g) was slowly added over 10 min with stirring and cooling. During this process, the temperature of the mixture was maintained below 293 K. The mixture was then heated to 308 K and stirred for 2 hours, and distilled water (160 ml) was added over 30 min. Next, the mixture was further diluted with distilled water (500 ml) and treated with 30% H_2O_2 (8.3 ml). After the suspension turned bright yellow, it was allowed to sit for 1 day, and the supernatant was then decanted. The residue was centrifuged and washed three times with 10% HCl (800 ml) at 3000 rpm. The residue was then centrifuged and washed with distilled water repeatedly until the pH of the rinse water reached a value of 6. For the preparation of GO in *N*,*N*-dimethyl formamide (DMF), the GO suspension was centrifuged at 15,000 rpm for 1 hour and the supernatant was then decanted. The residue was centrifuged and washed five times with DMF (Junsei; 99.5%; density, 0.952 g/ml) (40 ml) at 15,000 rpm for 1 hour. The PVDF (Sigma Aldrich; molecular weight, ~530,000, pellet) solution (10 wt % in DMF) was mixed with the GO/DMF suspension.

Device fabrication

The PVDF/GO nanocomposite films were fabricated by solution-based rod casting using a glass rod on the glass plate at 50°C and drying for 12 hours. The films were dried again in a vacuum oven at 160°C for 3 hours to remove the residual DMF solvent and reduce the GO into rGO. The residual DMF solvent was completely removed during the annealing process (fig. S17). A series of graphene/PVDF nanocomposite films with different graphene loadings were similarly prepared. To fabricate the interlocked microdome rGO/PVDF nanocomposite films, a PDMS replica mold was prefabricated by the double-casting method. The double-casting method was initiated by coating the water-soluble polymer poly(vinyl alcohol) (PVA) as a thin interlayer onto an as-prepared PDMS film fabricated by the micromolding of a silicon substrate with microdome patterns (10 μm in diameter, 12 μm in pitch, and 4 μm in height). The PDMS prepolymer was then poured onto the PVA-coated microdome-patterned PDMS film, after which the fully cured replica mold was peeled off along with the microdome arrays at 90°C for 3 hours. Finally, by removing the residual PVA on the surface of the PDMS replica mold by soaking in water, the fabrication of the replica mold was completed. Using the micromolding process, we prepared ferroelectric rGO/PVDF nanocomposite films with microdome arrays (fig. S18). The resulting films had the following feature sizes: diameter, 10 μm; pitch, 12 μm; and height, 4 μm. Before the micromolding of the GO/PVDF composite, we treated the prepared replica PDMS mold with oxygen plasma for 1 min to make the surface less adhesive to the hydrophobic GO/PVDF solution. The GO/PVDF precursor (500 μl) was then cast onto the oxygen plasma–treated replica mold and subsequently stored in a vacuum oven at 160°C for 6 hours. Finally, the fingerprint-inspired micropattern for texture perception was prepared by the PDMS micromolding process with regular dimensions of about 500 μm in pitch and 160 μm in ridge width. The thickness of the fingerprint-patterned PDMS film was 50 μm.

Characterization

Field-emission scanning electron microscopy (S-4800, Hitachi) was used to observe the morphology of the GO/PVDF composite films. Differential scanning calorimetry (DSC) measurements (DSC Q10, TA instrument) of the GO/PVDF nanocomposites were conducted under nitrogen gas in the 193 to 473 K temperature range with cooling/heating speeds of 20 K/min. The crystalline structure of GO/PVDF nanocomposites was determined using XRD (Rigaku Ultima IV) with CuK_α radiation. FTIR (NICOLET 380, Thermo Scientific) measurements were conducted to examine the changes in the bonding structure. The electrical properties of the rGO/PVDF nanocomposites under controlled temperatures were measured by a source meter (S-2400, Keithley). For the TCR measurements, the temperature of the hot stage was controlled by the Advanced Peltier System attached to ARES-G2 (TA Instruments).

Measurements of the sensing performance of the e-skins

To measure the electrical properties of the e-skin devices as a function of pressure and temperature variation, we attached two Cu electrodes to the top and bottom of the sandwiched microdome-patterned nanocomposite films (size, 1.5 cm × 1.5 cm) using silver paste and annealed them at 90°C for 1 hour to minimize contact resistance. A thin PDMS film (thickness, ~300 μm) was used as a supporting layer to fix the e-skin and reduce electrical noise. To measure the pressure-induced electrical properties, we collected piezoresistive and piezoelectric signals using a semiconductor parameter analyzer (4200-SCS, Keithley) and source meter (S-2400, Keithley), respectively. A static normal pressure was applied by the pushing tester (JIPT, JUNIL TECH) with a pushing speed of 3 mm/s as controlled moving displacement. For the frequency-dependent pressure measurements via piezoelectric sensors, the frequencies of applied pressure were modulated by varying the pushing speed (0.3 to 4.5 mm/s) under a fixed moving distance of the pushing tester (schematic illustration in fig. S19A). Here, the piezoelectric output signals were measured by a source meter with infinitely large input impedance (>10 gigohm). The number of power line cycles of 1 was used to increase the measurement resolution and accuracy. The e-skin (sensor size, 1 cm^2) was subjected to loading/unloading cycles of water-filled glass vials with different temperatures and pressures at 2-s intervals to evaluate the detection of simultaneous temperature and pressure variations. The wearable e-skin (sensor size, 1 cm^2) encapsulated by polyimide films on both sides was wrapped onto the wrist to monitor the variation in the artery pressure pulse. Changes in the artery pressure pulse with exercise and body temperature were monitored after running for 5 min and immersing the wrist in warm and cold water for 2 min. To evaluate the sensing of dynamic pressure, we used a speaker (SMS-A90, Samsung) connected to a frequency sound generator (APKCRAFT) to generate acoustic sound waves, which were dictated via an electronic dictionary (Oxford) program (fig. S19B). The sound waves (sound intensity, 96.5 dB) were

then applied to the e-skin using a speaker placed at a distance of 2 cm from the e-skin. The electrical voltage generated was analyzed by an oscilloscope (DPO 2022B, Tektronix). A spectrogram of the original acoustic waves was displayed by an audio editor program (WaveSurfer). To evaluate the perception of surface textures, we used a laboratory-built microstage system (Micro Motion Technology) for cyclic displacement within 1 cm at constant moving speeds (0.25 to 2.5 mm/s) and loading pressure (0.3 N). For this measurement, various target substrates such as PDMS substrates with parallel line patterns (D = 160 μm; P = 500 μm), sandpaper, glass, paper, and silicon substrates with different geometric patterns were used. For the discrimination of surface hardness/softness, the parallel line–patterned PDMS substrates with different moduli were prepared by adjusting the mixing ratio of PDMS base to curing agent (10:1, 15:1, and 20:1) (*68*).

SUPPLEMENTARY MATERIALS

Supplementary material for this article is available at http://advances.sciencemag.org/cgi/content/full/1/9/e1500661/DC1

Section 1. Ferroelectric crystalline structures in PVDF/GO composites.
Section 2. Local temperature equilibrium model for the water droplet on e-skins.
Section 3. Characteristic time to reach thermal equilibrium for the water droplet on e-skins.
Fig. S1. Phase transition of the GO/PVDF composite films with various thermal treatments.
Fig. S2. FTIR spectra of the GO/PVDF composite films with GO loading concentrations of 0, 1, and 5 wt %.
Fig. S3. Crystalline structures of PVDF at different phases.
Fig. S4. Cross-sectional SEM images, crystallinity, and mechanical properties of the rGO/PVDF composite films with various rGO loading concentrations.
Fig. S5. Relative resistance (R/R_0) variations of the e-skin (planar-structured rGO/PVDF composite film) after contact with the water droplet (temperature, 19.6°C).
Fig. S6. Relative resistance of e-skin as a function of the wide dynamic range of applied pressure from 10 to 49.5 kPa.
Fig. S7. Minimum pressure detection of ferroelectric e-skins.
Fig. S8. Stability of the piezoresistive pressure sensor under repetitive application and release of 25.5 kPa of pressure over 5000 cycles.
Fig. S9. Changes in the TCR and initial resistance values at different preloading weights.
Fig. S10. Effect of film conductivity on the piezoelectric outputs.
Fig. S11. Comparison of the piezoelectric and piezoresistive signal variations of e-skins in response to applied pressure with different frequencies (0.3 to 5.0 Hz).
Fig. S12. STFT spectrograms of the piezoelectric current signals for the high-frequency range (>80 Hz) obtained by scanning on PDMS films with periodic line patterns as a function of scanning speed.
Fig. S13. Effect of e-skin structure and fingerprint patterns for texture perception.
Fig. S14. Perception of hardness/softness of surface.
Fig. S15. Wearable e-skins for texture perception.
Fig. S16. Perception of fine textures for the low-frequency range (<30 Hz) obtained by scanning on PDMS films with periodic line patterns as a function of scanning speed.
Fig. S17. FTIR spectra for verifying residue solvent.
Fig. S18. Schematic illustrations of the double-casting and micromolding processes for the rGO/PVDF composite film with a microdome-patterned surface.
Fig. S19. Experimental setup for detection of dynamic pressure.

REFERENCES AND NOTES

1. T. Someya, Y. Kato, T. Sekitani, S. Iba, Y. Noguchi, Y. Murase, H. Kawaguchi, T. Sakurai, Conformable, flexible, large-area networks of pressure and thermal sensors with organic transistor active matrixes. *Proc. Natl. Acad. Sci. U.S.A.* **102**, 12321–12325 (2005).
2. T. Sekitani, T. Yokota, U. Zschieschang, H. Klauk, S. Bauer, K. Takeuchi, M. Takamiya, T. Sakurai, T. Someya, Organic nonvolatile memory transistors for flexible sensor arrays. *Science* **326**, 1516–1519 (2009).
3. K. Takei, T. Takahashi, J. C. Ho, H. Ko, A. G. Gillies, P. W. Leu, R. S. Fearing, A. Javey, Nanowire active-matrix circuitry for low-voltage macroscale artificial skin. *Nat. Mater.* **9**, 821–826 (2010).
4. S. C. B. Mannsfeld, B. C.-K. Tee, R. M. Stoltenberg, C. V. H.-H. Chen, S. Barman, B. V. O. Muir, A. N. Sokolov, C. Reese, Z. Bao, Highly sensitive flexible pressure sensors with microstructured rubber dielectric layers. *Nat. Mater.* **9**, 859–864 (2010).
5. D.-H. Kim, N. S. Lu, R. Ma, Y.-S. Kim, R.-H. Kim, S. D. Wang, J. Wu, S. M. Won, H. Tao, A. Islam, K. J. Yu, T.-. Kim, R. Chowdhury, M. Ying, L. Z. Xu, M. Li, H.-J. Chung, H. Keum, M. McCormick, P. Liu, Y.-W. Zhang, F. G. Omenetto, Y. Huang, T. Coleman, J. A. Rogers, Epidermal electronics. *Science* **333**, 838–843 (2011).
6. C. Pang, G.-Y. Lee, T.-. Kim, S. M. Kim, H. N. Kim, S.-H. Ahn, K.-Y. Suh, A flexible and highly sensitive strain-gauge sensor using reversible interlocking of nanofibres. *Nat. Mater.* **11**, 795–801 (2012).
7. F.-R. Fan, L. Lin, G. Zhu, W. Z. Wu, R. Zhang, Z. L. Wang, Transparent triboelectric nanogenerators and self-powered pressure sensors based on micropatterned plastic films. *Nano Lett.* **12**, 3109–3114 (2012).
8. C. Wang, D. Hwang, Z. Yu, K. Takei, J. Park, T. Chen, B. W. Ma, A. Javey, User-interactive electronic skin for instantaneous pressure visualization. *Nat. Mater.* **12**, 899–904 (2013).
9. M. Kaltenbrunner, T. Sekitani, J. Reeder, T. Yokota, K. Kuribara, T. Tokuhara, M. Drack, R. Schwödiauer, I. Graz, S. Bauer-Gogonea, S. Bauer, T. Someya, An ultra-lightweight design for imperceptible plastic electronics. *Nature* **499**, 458–463 (2013).
10. W. Wu, X. Wen, Z. L. Wang, Taxel-addressable matrix of vertical-nanowire piezotronic transistors for active and adaptive tactile imaging. *Science* **340**, 952–957 (2013).
11. R. C. Webb, A. P. Bonifas, A. Behnaz, Y. Zhang, K. J. Yu, H. Cheng, M. Shi, Z. Bian, Z. Liu, Y.-S. Kim, W.-H. Yeo, J. S. Park, J. Song, Y. Li, Y. Huang, A. M. Gorbach, J. A. Rogers, Ultrathin conformal devices for precise and continuous thermal characterization of human skin. *Nat. Mater.* **12**, 938–944 (2013).
12. S. Gong, W. Schwalb, Y. Wang, Y. Chen, Y. Tang, J. Si, B. Shirinzadeh, W. Cheng, A wearable and highly sensitive pressure sensor with ultrathin gold nanowires. *Nat. Commun.* **5**, 3132 (2014).
13. K. Takei, Z. Yu, M. Zheng, H. Ota, T. Takahashi, A. Javey, Highly sensitive electronic whiskers based on patterned carbon nanotube and silver nanoparticle composite films. *Proc. Natl. Acad. Sci. U.S.A.* **111**, 1703–1707 (2014).
14. L. Pan, A. Chortos, G. Yu, Y. Wang, S. Isaacson, R. Allen, Y. Shi, R. Dauskardt, Z. Bao, An ultra-sensitive resistive pressure sensor based on hollow-sphere microstructure induced elasticity in conducting polymer film. *Nat. Commun.* **5**, 3002 (2014).
15. S. Bauer, S. Bauer-Gogonea, I. Graz, M. Kaltenbrunner, C. Keplinger, R. Schwödiauer, 25th anniversary article: A soft future: From robots and sensor skin to energy harvesters. *Adv. Mater.* **26**, 149–162 (2014).
16. J. Kim, M. Lee, H. J. Shim, R. Ghaffari, H. R. Cho, D. Son, Y. H. Jung, M. Soh, C. Choi, S. Jung, T. Hyeon, D.-H. Kim, Stretchable silicon nanoribbon electronics for skin prosthesis. *Nat. Commun.* **5**, 5747 (2014).
17. D. Son, J. Lee, S. Qiao, R. Ghaffari, J. Kim, J. E. Lee, C. Song, S. J. Kim, D. J. Lee, S. W. Jun, S. Yang, M. Park, J. Shin, K. Do, M. Lee, K. Kang, C. S. Hwang, N. Lu, T. Hyeon, D.-H. Kim, Multifunctional wearable devices for diagnosis and therapy of movement disorders. *Nat. Nanotechnol.* **9**, 397–404 (2014).
18. W.-H. Yeo, Y.-S. Kim, J. Lee, A. Ameen, L. Shi, M. Li, S. Wang, R. Ma, S. H. Jin, Z. Kang, Y. Huang, J. A. Rogers, Multifunctional epidermal electronics printed directly onto the skin. *Adv. Mater.* **25**, 2773–2778 (2013).
19. L. Xu, S. R. Gutbrod, A. P. Bonifas, Y. Su, M. S. Sulkin, N. Lu, H.-J. Chung, K.-I. Jang, Z. Liu, M. Ying, C. Lu, R. C. Webb, J.-S. Kim, J. I. Laughner, H. Cheng, Y. Liu, A. Ameen, J.-W. Jeong, G.-T. Kim, Y. Huang, I. R. Efimov, J. A. Rogers, 3D multifunctional integumentary membranes for spatiotemporal cardiac measurements and stimulation across the entire epicardium. *Nat. Commun.* **5**, 3329 (2014).
20. N. T. Tien, S. Jeon, D.-I. Kim, T. Q. Trung, M. Jang, B.-U. Hwang, K.-E. Byun, J. Bae, E. Lee, J. B.-H. Tok, Z. Bao, N.-E. Lee, J.-J. Park, A flexible bimodal sensor array for simultaneous sensing of pressure and temperature. *Adv. Mater.* **26**, 796–804 (2014).
21. C. Hou, H. Wang, Q. Zhang, Y. Li, M. Zhu, Highly conductive, flexible, and compressible all-graphene passive electronic skin for sensing human touch. *Adv. Mater.* **26**, 5018–5024 (2014).
22. I. Graz, M. Krause, S. Bauer-Gogonea, S. Bauer, S. P. Lacour, B. Ploss, M. Zirkl, B. Stadlober, S. Wagner, Flexible active-matrix cells with selectively poled bifunctional polymer-ceramic nanocomposite for pressure and temperature sensing skin. *J. Appl. Phys.* **106**, 034503 (2009).
23. R. D. Howe, M. R. Cutkosky, Dynamic tactile sensing: Perception of fine surface features with stress rate sensing. *IEEE Trans. Robot. Autom.* **9**, 140–151 (1993).
24. J. Dargahi, S. Najarian, Human tactile perception as a standard for artificial tactile sensing—A review. *Int. J. Med. Robot. Comp.* **1**, 23–35 (2004).
25. P. Delmas, J. Hao, L. Rodat-Despoix, Molecular mechanisms of mechanotransduction in mammalian sensory neurons. *Nat. Rev. Neurosci.* **12**, 139–153 (2011).
26. J. Scheibert, S. Leurent, A. Prevost, G. Debrégeas, The role of fingerprints in the coding of tactile information probed with a biomimetic sensor. *Science* **323**, 1503–1506 (2009).
27. R. Fagiani, F. Massi, E. Chatelet, Y. Berthier, A. Akay, Tactile perception by friction induced vibrations. *Tribol. Int.* **44**, 1100–1110 (2011).
28. E. Wandersman, R. Candelier, G. Debrégeas, A. Prevost, Texture-induced modulations of friction force: The fingerprint effect. *Phys. Rev. Lett.* **107**, 164301 (2011).
29. N. Cauna, Nature and functions of the papillary ridges of the digital skin. *Anat. Rec.* **119**, 449–468 (1954).

30. R. S. Dahiya, G. Metta, M. Valle, G. Sandini, Tactile sensing—From humans to humanoids. *IEEE Trans. Robot.* **26**, 1–20 (2010).
31. H. Athenstaedt, Permanent longitudinal electric polarization and pyroelectric behaviour of collagenous structures and nervous tissue in man and other vertebrates. *Nature* **228**, 830–834 (1970).
32. H. Athenstaedt, H. Claussen, D. Schaper, Epidermis of human skin: Pyroelectric and piezoelectric sensor layer. *Science* **216**, 1018–1020 (1982).
33. D. De Rossi, A. Nannini, C. Domenici, Artificial sensing skin mimicking mechanoelectrical conversion properties of human dermis. *IEEE Trans. Biomed. Eng.* **35**, 83–92 (1988).
34. J. Park, Y. Lee, J. Hong, M. Ha, Y.-D. Jung, H. Lim, S. Y. Kim, H. Ko, Giant tunneling piezoresistance of composite elastomers with interlocked microdome arrays for ultrasensitive and multimodal electronic skins. *ACS Nano* **8**, 4689–4697 (2014).
35. J. Park, Y. Lee, J. Hong, Y. Lee, M. Ha, Y. Jung, H. Lim, S. Y. Kim, H. Ko, Tactile-direction-sensitive and stretchable electronic skins based on human-skin-inspired interlocked microstructures. *ACS Nano* **8**, 12020–12029 (2014).
36. V. Sencadas, S. Lanceros-Méndez, J. F. Mano, Characterization of poled and non-poled β-PVDF films using thermal analysis techniques. *Thermochim. Acta* **424**, 201–207 (2004).
37. X. J. He, J. H. Du, Z. Ying, H. M. Cheng, X. J. He, Positive temperature coefficient effect in multiwalled carbon nanotube/high-density polyethylene composites. *Appl. Phys. Lett.* **86**, 062112 (2005).
38. J. Meyer, Stability of polymer composites as positive-temperature-coefficient resistors. *Polym. Eng. Sci.* **14**, 706–716 (1974).
39. H. Pang, Y.-C. Zhang, T. Chen, B.-Q. Zeng, Z.-M. Li, Tunable positive temperature coefficient of resistivity in an electrically conducting polymer/graphene composite. *Appl. Phys. Lett.* **96**, 251907 (2010).
40. S. Ansari, E. P. Giannelis, Functionalized graphene sheet—Poly(vinylidene fluoride) conductive nanocomposites. *J. Polym. Sci. Pt. B Polym. Phys.* **47**, 888–897 (2009).
41. I. Jung, D. A. Dikin, R. D. Piner, R. S. Ruoff, Tunable electrical conductivity of individual graphene oxide sheets reduced at "low" temperatures. *Nano Lett.* **8**, 4283–4287 (2008).
42. M. E. Itkis, F. Borondics, A. Yu, R. C. Haddon, Bolometric infrared photoresponse of suspended single-walled carbon nanotube films. *Science* **312**, 413–416 (2006).
43. R. Lu, C. Christianson, B. Weintrub, J. Z. Wu, High photoresponse in hybrid graphene–carbon nanotube infrared detectors. *ACS Appl. Mater. Interfaces* **5**, 11703–11707 (2013).
44. M. Tian, Y. Huang, W. Wang, R. Li, P. Liu, C. Liu, Y. Zhang, Temperature-dependent electrical properties of graphene nanoplatelets film dropped on flexible substrates. *J. Mater. Res.* **29**, 1288–1294 (2014).
45. J. N. Cohn, S. Finkelstein, G. Mcveigh, D. Morgan, L. Lemay, J. Robinson, J. Mock, Noninvasive pulse wave analysis for the early detection of vascular disease. *Hypertension* **26**, 503–508 (1995).
46. W. B. White, L. Wolfson, C. Guttman, N. Moscufo, D. Wakefield, R. Kaplan, G. Pearlson, Average daily blood pressure, not office blood pressure, determines the progression of cerebrovascular disease and functional decline in older persons. *J. Am. Coll. Cardiol.* **57**, E490 (2011).
47. G. Schwartz, B. C.-K. Tee, J. Mei, A. L. Appleton, D. H. Kim, H. Wang, Z. Bao, Flexible polymer transistors with high pressure sensitivity for application in electronic skin and health monitoring. *Nat. Commun.* **4**, 1859 (2013).
48. L. Y. Chen, B. C.-K. Tee, A. L. Chortos, G. Schwartz, V. Tse, D. J. Lipomi, H.-S. P. Wong, M. V. McConnell, Z. Bao, Continuous wireless pressure monitoring and mapping with ultra-small passive sensors for health monitoring and critical care. *Nat. Commun.* **5**, 5028–5037 (2014).
49. Z. T. Li, Z. L. Wang, Air/liquid-pressure and heartbeat-driven flexible fiber nanogenerators as a micro/nano-power source or diagnostic sensor. *Adv. Mater.* **23**, 84–89 (2011).
50. X. Wang, Y. Gu, Z. Xiong, Z. Cui, T. Zhang, Silk-molded flexible, ultrasensitive, and highly stable electronic skin for monitoring human physiological signals. *Adv. Mater.* **26**, 1336–1342 (2014).
51. C. Dagdeviren, Y. Su, P. Joe, R. Yona, Y. Liu, Y.-S. Kim, Y. Huang, A. R. Damadoran, J. Xia, L. W. Martin, Y. Huang, J. A. Rogers, Conformable amplified lead zirconate titanate sensors with enhanced piezoelectric response for cutaneous pressure monitoring. *Nat. Commun.* **5**, 4496 (2014).
52. C.-M. Huang, H.-C. Chang, S.-T. Kao, T.-C. Li, C.-C. Wei, C. Chen, Y.-T. Liao, F.-J. Chen, Radial pressure pulse and heart rate variability in heat- and cold-stressed humans. *Evid. Based Complement. Alternat. Med.* **2011**, 751317 (2011).
53. W. W. Nichols, Clinical measurement of arterial stiffness obtained from noninvasive pressure waveforms. *Am. J. Hypertens.* **18**, 3S–10S (2005).
54. S. Munir, B. Y. Jiang, A. Guilcher, S. Brett, S. Redwood, M. Marber, P. Chowienczyk, Exercise reduces arterial pressure augmentation through vasodilation of muscular arteries in humans. *Am. J. Physiol. Heart Circ. Physiol.* **294**, H1645–H1650 (2008).
55. J. O. Godden, G. M. Roth, E. A. Hines Jr., J. F. Schlegel, The changes in the intra-arterial pressure during immersion of the hand in ice-cold water. *Circulation* **12**, 963–973 (1955).
56. M.-L. Seol, H. Im, D.-I. Moon, J.-H. Woo, D. Kim, S.-J. Choi, Y.-K. Choi, Design strategy for a piezoelectric nanogenerator with a well-ordered nanoshell array. *ACS Nano* **7**, 10773–10779 (2013).
57. H. Yu, T. Huang, M. Lu, M. Mao, Q. Zhang, H. Wang, Enhanced power output of an electrospun PVDF/MWCNTs-based nanogenerator by tuning its conductivity. *Nanotechnology* **24**, 405401 (2013).
58. L. Huang, C. Lu, F. Wang, L. Wang, Preparation of PVDF/graphene ferroelectric composite films by in situ reduction with hydrobromic acids and their properties. *RSC Adv.* **4**, 45220–45229 (2014).
59. M. El Achaby, F. Z. Arrakhiz, S. Vaudreuil, E. M. Essassi, A. Qaiss, M. Bousmina, Preparation and characterization of melt-blended graphene nanosheets–poly (vinylidene fluoride) nanocomposites with enhanced properties. *J. Appl. Polym. Sci.* **127**, 4697–4707 (2013).
60. J. Sirohi, I. Chopra, Fundamental understanding of piezoelectric strain sensors. *J. Intell. Mater. Syst. Struct.* **11**, 246–257 (2000).
61. C. Chang, V. H. Tran, J. Wang, Y.-K. Fuh, L. Lin, Direct-write piezoelectric polymeric nanogenerator with high energy conversion efficiency. *Nano Lett.* **10**, 726–731 (2010).
62. L. Gu, N. Cui, L. Cheng, Q. Xu, S. Bai, M. Yuan, W. Wu, J. Liu, Y. Zhao, F. Ma, Y. Qin, Z. L. Wang, Flexible fiber nanogenerator with 209 V output voltage directly powers a light-emitting diode. *Nano Lett.* **13**, 91–94 (2012).
63. L. Persano, C. Dagdeviren, Y. Su, Y. Zhang, S. Girardo, D. Pisignano, Y. Huang, J. A. Rogers, High performance piezoelectric devices based on aligned arrays of nanofibers of poly(vinylidenefluoride-co-trifluoroethylene). *Nat. Commun.* **4**, 1633 (2013).
64. A. Prevost, J. Scheibert, G. Debrégeas, Effect of fingerprints orientation on skin vibrations during tactile exploration of textured surfaces. *Commun. Integr. Biol.* **2**, 422–424 (2009).
65. M. Wiertlewski, C. Hudin, V. Hayward, On the 1/f noise and non-integer harmonic decay of the interaction of a finger sliding on flat and sinusoidal surfaces, in *2011 World Haptics Conference* (2011), pp. 25–30.
66. S. J. Bensmaïa, M. Hollins, The vibrations of texture. *Somatosens. Mot. Res.* **20**, 33–43 (2003).
67. M. C. Audry, C. Fretigny, A. Chateauminois, J. Teissere, E. Barthel, Slip dynamics at a patterned rubber/glass interface during stick-slip motions. *Eur. Phys. J. E* **35**, 83–89 (2012).
68. D. S. Um, S. Lim, Y. Lee, H. Lee, H. J. Kim, W. C. Yen, Y. L. Chueh, H. Ko, Vacuum-induced wrinkle arrays of InGaAs semiconductor nanomembranes on polydimethylsiloxane microwell arrays. *ACS Nano* **8**, 3080–3087 (2014).

Acknowledgments: We thank Y. Lee, S. Lim, and H. Ham for their assistance with drawing illustrations, fabrication of silicon patterns, and preparation of PVDF/GO precursors, respectively. **Funding:** This work was supported by the National Research Foundation of Korea (NRF-2011-0014965 and NRF-2014M3C1B2048198), the Center for Advanced Soft Electronics funded by the Ministry of Science, ICT and Future Planning as Global Frontier Project (NRF-2015M3A6A5065314), and the Graphene Materials/Components Development Project (10044366) funded by the Ministry of Trade, Industry & Energy (Korea). **Author contributions:** H.K. and H.S.L. conceived the project. J.P., M.K., H.S.L., and H.K. designed the experiments. J.P., M.K., and Y.L. performed the experiments. J.P., M.K., Y.L., H.S.L., and H.K. analyzed the data. J.P., M.K., H.S.L., and H.K. wrote the manuscript, to which all authors provided feedback. **Competing interests:** The authors declare that they have no competing interests. **Data and materials availability:** All data needed to evaluate the conclusions in the paper are present in the paper and/or the Supplementary Materials. Additional data related to this paper are available from the authors upon request.

Submitted 22 May 2015
Accepted 13 September 2015
Published 30 October 2015
10.1126/sciadv.1500661

Citation: J. Park, M. Kim, Y. Lee, H. S. Lee, H. Ko, Fingertip skin–inspired microstructured ferroelectric skins discriminate static/dynamic pressure and temperature stimuli. *Sci. Adv.* **1**, e1500661 (2015).